


# Adaptive quantum tomography in an indistinct measurement system with superconducting circuits

Hyeok Hwang<sup>✉</sup>, JaeKyung Choi<sup>✉</sup>, and Eunseong Kim<sup>\*</sup>

*Department of Physics, Korea Advanced Institute of Science and Technology (KAIST), Republic of Korea*

 (Received 2 June 2023; revised 1 September 2023; accepted 2 November 2023; published 5 December 2023; corrected 28 December 2023)

Adaptive tomography has been widely investigated with the aim of achieving faster state tomography processing of quantum systems. Infidelity of the nearly pure states in a quantum information process generally scales as  $O(1/\sqrt{N})$ , which requires a large number of statistical ensembles in comparison to the infidelity scaling of  $O(1/N)$  for mixed states. One previous report optimized the measurement basis in a photonic qubit system, whose state tomography uses projective measurements, to obtain an infidelity scaling of  $O(1/N)$ . However, this dramatic improvement cannot be applied to indistinct measurement systems in which two quantum states cannot be distinguished with perfect measurement fidelity. We introduce in this work an optimal measurement basis to achieve fast adaptive quantum state tomography and a minimum magnitude of infidelity in an indistinct measurement system. We expect that the adaptive quantum state tomography protocol can lead to a reduction in the number of required measurements of approximately 33.74% via analytical expectation without changing the  $O(1/\sqrt{N})$  scaling. Experimentally, we find a 15.06% measurement number reduction in a superconducting circuit system.

DOI: [10.1103/PhysRevApplied.20.064007](https://doi.org/10.1103/PhysRevApplied.20.064007)

## I. INTRODUCTION

Quantum state tomography (QST) is a procedure for finding an adequate description of a quantum state based on tomographic data collected from a series of measurements [1–19]. For example, a goal of QST may be to identify an estimator ( $\hat{\rho}$ ) that describes the state of a qubit ( $\rho$ ). Various approaches to optimize QST have been studied both in the direction of finding reasonable estimators from given tomographic data and in the direction of modifying the sampling strategies applied to obtain the tomographic data.

Several different approaches to the identification of a quantum state from tomographic data have been investigated for decades. One example is direct inversion tomography, which designates the most probable state as the estimator for given tomographic data [5]. However, the resulting estimator from this method can be an unphysical state (outside the Bloch sphere) due to statistical uncertainty. Another example approach is maximum likelihood estimation, which refines the probabilistic interpretation of direct inversion tomography by limiting the possible range of qubit state vectors to the inside of the Bloch sphere; in this case, though, the maximum of the likelihood function may not be unique, which is known as rank deficiency [2,5,8,12,13,15,16,20–22]. To eliminate this rank-deficient

property of the likelihood function, a third approach to the identification of a quantum state from tomographic data is Bayesian mean estimation [5,9,20,22–24], which interprets the likelihood function as a weighting factor for a given density operator. As the resulting estimator from Bayesian mean estimation is never rank deficient, this approach is widely used for QST. In terms of sampling strategies for tomographic data, in addition to using Cartesian axes, the use of four axes passing through the vertices of a tetrahedron has been investigated [9,25], for example. But because estimators converge at different rates depending on the quantum state [5,13,20,21,26], a fixed set of sampling axes is not optimal for every quantum state simultaneously. To overcome this limitation, strategies to construct optimal measurement axes from prior information on quantum states have been suggested, which are known as adaptive quantum state tomography (AQST) [20,21,23–28].

Theoretical methodologies for AQST have focused on optimizing measurement configurations, utilizing mutually unbiased observables [13,29], and expanding the number of adaption steps [26]. In addition, experimental realizations of AQST have been reported in measurement systems with sufficiently high measurement fidelity [20,21,23,24,26]. Despite this progress, one area that is relatively less explored is the experimental realization of AQST for measurement systems with indistinct measurement fidelity, which are systems that acquire partial

<sup>\*</sup>eunseong@kaist.edu

information on observables through state-entangled classical fields [30–33]. Considering the recent spotlight on superconducting circuit systems [18,19,33–41], the cavity’s photon response, which varies depending on the qubit’s state, is utilized to measure the qubit’s state. We suggest in this work a methodology for AQST in a transmon qubit system [40,42,43], which is one of the most widely investigated segments of superconducting circuit systems.

Several kinds of metrics, such as infidelity [5,12,13,20,21,26], can quantify the estimation error in QST. Because these metrics are related to the power of the estimation error, the proposed AQST approach employs an estimation error variance that is dependent on the state of a qubit to minimize the estimation error variance. The process involves two stages: a relatively small number of ensembles are initially measured to provide a rough estimation of the state of a qubit, and then a large number of ensembles are measured to obtain a precise estimation after applying a feedback drive to minimize variance. The reduction in the number of measurements required to achieve a specific error bound is related to the change in this variance. Hence, we depict the effectiveness of our AQST by comparing the relation between the number of measurements versus the variance of the measured data of our AQST case to that of a standard QST case with both analytical expectation and experiment. We find a remarkable reduction in the number of measurements required to get a specific error, and thus expect that the AQST process can offer advantages in state readout.

## II. RESULT

Several metrics can be used to quantify the difference between the qubit state  $\rho$  and the estimator  $\hat{\rho}$  from QST. Example metrics include the Hilbert-Schmidt distance  $d_{\text{HS}}(\rho, \hat{\rho}) = [\text{Tr}(\rho - \hat{\rho})^2]^{1/2}$ , which is related to the probability of obtaining the estimator  $\hat{\rho}$  from given qubit state  $\rho$ ; the trace distance  $d_{\text{tr}}(\rho, \hat{\rho}) = \text{Tr}|\rho - \hat{\rho}|$ , which is related to single-shot error; and the infidelity  $1 - F(\rho, \hat{\rho}) = 1 - \text{Tr}[\sqrt{\sqrt{\rho}\hat{\rho}\sqrt{\rho}}]^2$ , which is frequently used not only for its sensitivity but also for its physical meaning for pure state cases [5,12,13,20,21,26]. These metrics are proportional to the power of the estimation error  $\Delta_\rho = \rho - \hat{\rho}$  [12,20], so minimizing the variance of  $\Delta$  is a main concern of QST. Therefore, we studied the statistics of the variance of  $\Delta$  as follows.

To find the relation between estimation error  $\Delta$  and tomographic data, the relation between point  $\vec{p}$  in probability space  $P$  and point  $\vec{r}$  in Bloch space  $B$  needs to be checked. The probability of getting a measurement outcome corresponding to  $j$  for qubit state  $\rho = |i\rangle\langle i|$  is denoted by  $P_i^j$  ( $i \in \{g, e\}, j \in \{0, 1\}$ ). Both  $P_g^0$  and  $P_e^1$  mean the fidelity of measurement, while both  $P_g^1$  and  $P_e^0$  mean

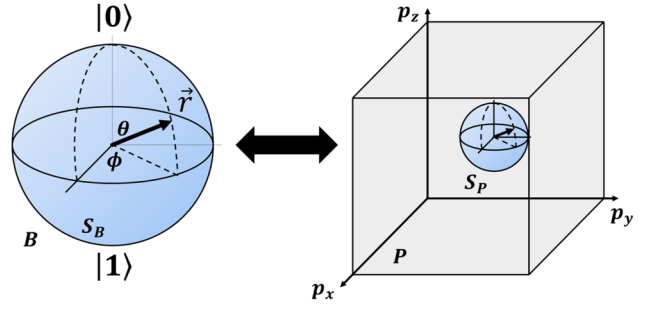


FIG. 1. The quantum state of a qubit can be described as a point  $\vec{r}$  on sphere  $S_B$  in Bloch space  $B$  (left). By mapping  $S_B$  to cubic probability space  $P$ , the point  $\vec{p} = \sum_k p_k \vec{k}$  can represent quantum state tomography (QST) data along three axes (right), where  $p_k$  is defined as the probability of measuring 0 along the  $k$  axis ( $k = x, y, z$ ). The states of the Bloch sphere  $S_B \subset B$  have a one-to-one correspondence with the sphere  $S_P \subset P$ .

the error of measurement. Whether the measurement outcome belongs to 0 or 1 depends on the classification criterion between 0 and 1, and thus the probability  $P_i^j$  also depends on the classification criterion. We denoted the probability of measuring 0 along the  $k$  axis ( $k = x, y, z$ ) as  $p_k = P_g^0 \text{Tr}(\hat{P}_g \rho_k) + P_e^0 \text{Tr}(\hat{P}_e \rho_k)$ , where  $\hat{P}_i = |i\rangle\langle i|$  ( $i = g, e$ ) and  $\rho_k$  is a rotated density operator to get the projected information along the  $k$  axis defined in Eq. (A2). The vector  $\sum_{k=x,y,z} p_k \vec{k}$  resides in cubic probability space  $P = \{(x, y, z) | 0 \leq x, y, z \leq 1\}$  (Fig. 1).

A quantum state of a qubit  $|\psi\rangle = \cos\theta|g\rangle + e^{i\phi}\sin\theta|e\rangle$  can be represented as the point  $\vec{r} = (r_x, r_y, r_z)$  in Bloch space  $B$ . We represent the relation between  $r_k$  and  $p_k$  as  $p_k = (\alpha_+ + \alpha_- r_k)/2$ , where  $\alpha_\pm = P_g^0 \pm P_e^0$ ,  $P_e^0 \leq p_k \leq P_g^0$ . Because tomographic data follow a binomial distribution  $X_k \sim B(n, p_k)$  along each  $k$  axis, for an estimator represented as  $\hat{p} = (p_x, p_y, p_z)$  with  $\hat{p}_k = X_k/(N/3)$ , the mean and standard deviation of  $\hat{p}$  can be found as follows:

$$\begin{aligned} X_k &\sim B(N/3, p_k) \\ \rightarrow m(X_k) &= (N/3)p_k, \sigma(X_k) = \sqrt{(N/3)p_k(1-p_k)} \\ \rightarrow m(\hat{p}_k) &= p_k, \sigma(\hat{p}_k) = \sqrt{\frac{p_k(1-p_k)}{N/3}}. \end{aligned} \quad (1)$$

According to the above representation of the standard deviation,  $\sigma(\hat{p}_k)$  scales as  $O(N^{-1/2})$  except for extreme cases when  $p_k$  or  $1-p_k$  scales as  $O(N^{-1})$  [21]. Then we may consider the case where  $p_k$  is not close to 0 or 1. When the fidelity of a measurement does not satisfy  $1 - P_g^0 = O(N^{-1})$ ,  $p_k$  cannot be close to 0 or 1.

One objective of our AQST methodology is to minimize the above standard deviation of  $\Delta = \hat{r} - \vec{r}$ , where

$$|\Delta| = \left| \sum_k \vec{k}(\hat{r}_k - r_k) \right| = \frac{2}{\alpha_-} \left| \sum_k \vec{k}(\hat{p}_k - p_k) \right|. \quad (2)$$

Every measurement is an independent event, so the variance of the estimation error is

$$\begin{aligned}\sigma^2(\Delta) &= \sigma^2\left(\frac{2}{\alpha_-}\sum_k \vec{k}(\hat{p}_k - p_k)\right) \\ &= \frac{4}{\alpha_-^2}\sum_k \frac{p_k(1-p_k)}{N/3} = \frac{12}{N\alpha_-^2}\left(\frac{3}{4} - |\vec{R}|^2\right).\end{aligned}\quad (3)$$

Therefore, the variance  $\sigma^2(\Delta)$  is represented as a function of  $\vec{R} \equiv \sum \vec{k}(p_k - 1/2) = |\vec{p} - \overrightarrow{OP}_O|$ , which is the difference between estimator  $\vec{p} \in P$  and  $P_O(1/2, 1/2, 1/2)$ , by the orthogonality of our measurement axes.

Let us consider a Bloch sphere mapped into probability space denoted by  $S_P$ . The sphere is constructed by vectors  $\vec{p} = (\alpha_+ + \alpha_- r_k)/2$ , so the center of the sphere  $S_P$  is  $S_{P_O}(\alpha_+/2, \alpha_+/2, \alpha_+/2)$ . Because  $\alpha_+$  is naturally larger than 1 due to relaxation, the center of the Bloch sphere is closer to  $(1, 1, 1)$  than to  $(0, 0, 0)$ . This means that the distance  $|\vec{R}|$  from a point in the Bloch sphere to  $P_O$  is minimized when  $\vec{p} = ((\alpha_+ - \alpha_-/\sqrt{3})/2)(1, 1, 1) = V_{\max}$  and maximized when  $\vec{p} = ((\alpha_+ + \alpha_-/\sqrt{3})/2)(1, 1, 1) = V_{\min}$  in the probability space (see Fig. 2).

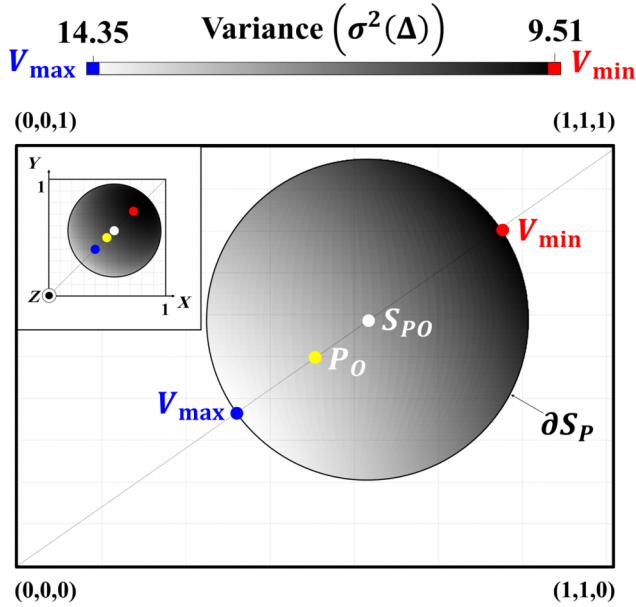


FIG. 2. Variance color map of qubit states on  $S_P$  with  $\alpha_+ = 1.178$ ,  $\alpha_- = 0.764$  is represented in the cross section of probability space  $P$  into the plane passing through the four vertices shown in the figure. The centers of  $P$  and  $S_P$  are denoted by  $P_O$  and  $S_{P_O}$ , respectively. According to Eq. (2), the variance of the estimator has a minimum and maximum value at  $V_{\min}$  and  $V_{\max}$ , which are the farthest and nearest points on  $S_P$  from point  $P_O$ , respectively. The four points mentioned are on the line connecting  $(0, 0, 0)$  and  $(1, 1, 1)$ . The inset represents the variance shown from the positive  $z$  axis.

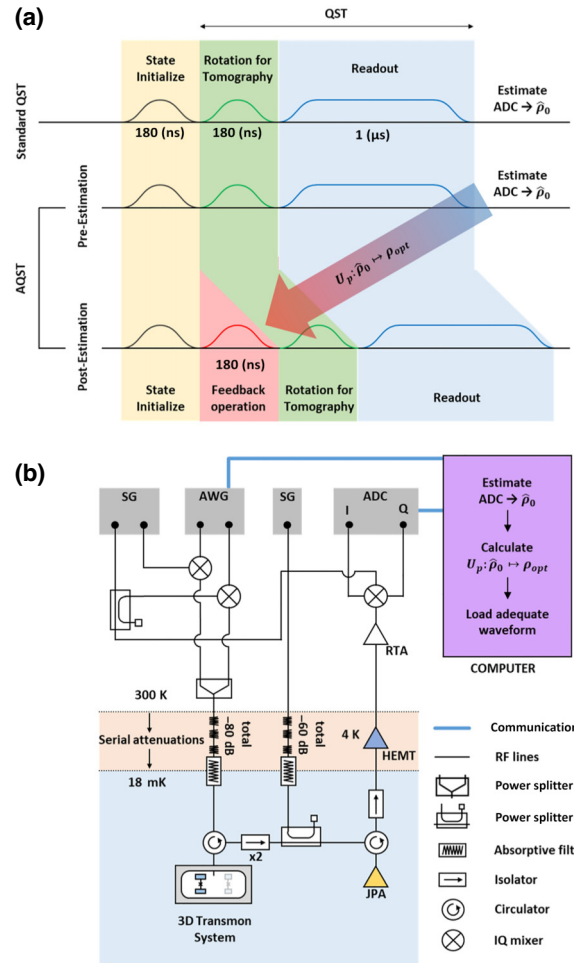


FIG. 3. Overview of the proposed AQST method. (a) Comparison of the standard QST process and proposed AQST process consisting of two steps. Preestimation is first implemented where a relatively small number of measurements are collected by an analog-to-digital converter (ADC) and used to find the first estimator  $\hat{\rho}_0$ . We calculate the adequate feedback function  $U_p$  to transform  $\hat{\rho}_0$  to  $\rho_{\text{opt}}$ , where  $\rho_{\text{opt}}$  is  $|\psi_{\text{best}}\rangle\langle\psi_{\text{best}}|$  in our AQST process. Postestimation is then implemented via the calculated feedback operation with a relatively large number of measurements. The result is a reduced estimation error from the same number of measurements. (b) Schematic of our experimental setup. A three-dimensional transmon qubit is mounted in an Al cavity on a mixing chamber stage at 18 mK in a dilution refrigerator. The output signal is amplified by three amplifiers: a Josephson parametric amplifier (JPA), high electron mobility transistor (HEMT), and room temperature amplifier (RTA) at 18 mK, 4 K, and 300 K, respectively. The feedback operation illustrated in (a) is calculated from the data collected by preestimation by computer, and the resulting pulse sequence corresponding to the calculated feedback operation is loaded to an arbitrary waveform generator (AWG).

According to Eq. (3), the larger  $\vec{R}$  is, the smaller the variance is. In other words, the minimum variance of  $\Delta$  can be achieved by maximizing the difference  $|\vec{R}|$ . The

relation between the qubit state and the minimum variance of  $\Delta$  is depicted in Fig. 2. The qubit estimator for the minimum and maximum variance is depicted as  $V_{\min}$  (red) and  $V_{\max}$  (blue), respectively. If we have information about the qubit state from a small number of QST data, by providing feedback that forces the qubit to be in the state corresponding to  $V_{\min}$ , the variance of the QST can be minimized; see Appendix A for details.

Based on the above discussion, we suggest an AQST process consisting of two steps, namely pre- and postestimation, which reduces the standard deviation of tomographic data by providing adaptive feedback in an indistinct measurement apparatus. Schematics of the proposed method and our experimental setup are illustrated in Fig. 3. With the AQST method, the  $O(N^{-1/2})$  scaling of the standard deviation of the data as in standard QST cases is conserved, but the magnitude of the standard deviation is minimized through geometrical optimization in Bloch space.

We use a three-dimensional transmon qubit as implemented in Fig. 3(b). The transmon qubit, with a transition frequency of 5.7957 GHz, is mounted in a 5.0724 GHz Al superconducting cavity with a coupling strength of  $g/2\pi = 28.21$  MHz and a Stark shift of  $\chi/2\pi = 1.100$  MHz; see Appendix B for details. The qubit relaxation time  $T_1$  is 3.0309  $\mu\text{s}$  and decoherence time  $T_2$  is 1.3503  $\mu\text{s}$ . The linewidth of the cavity  $\kappa/2\pi$  is 0.7205 MHz. We conduct each qubit state readout with microwave pulses in a heterodyne detection scheme (Fig. 3). The length of the control pulse is 180 ns for each rotation, and the length of the measurement pulse is 1  $\mu\text{s}$ , which gives the maximum distinguishability of  $|g\rangle$  and  $|e\rangle$  in the IQ plane; see Appendices C and D for details.

We prepare an ensemble of qubits in  $|\psi\rangle_{\text{worst}}$  (the furthest point from the origin), which is a state corresponding to  $V_{\max}$  (the closest point from the origin), and implement AQST by providing feedback to  $|\psi\rangle_{\text{best}}$ , which is a state corresponding to  $V_{\min}$ . The parameters of our system are summarized in Table I. The states  $|\psi\rangle_{\text{worst}}$  and  $|\psi\rangle_{\text{best}}$  can be calculated as follows:

$$\begin{aligned} |\psi_{\text{worst}}\rangle &= \sqrt{\frac{3-\sqrt{3}}{2}}|0\rangle + e^{i\frac{5\pi}{4}}\sqrt{\frac{3+\sqrt{3}}{2}}|1\rangle, \\ |\psi_{\text{best}}\rangle &= \sqrt{\frac{3+\sqrt{3}}{2}}|0\rangle + e^{i\frac{\pi}{4}}\sqrt{\frac{3-\sqrt{3}}{2}}|1\rangle. \end{aligned} \quad (4)$$

TABLE I. Parameters of our transmon system (up to significant figures).

$\omega_c/2\pi$ [GHz]	$\omega_q^{01}/2\pi$ [GHz]	$(\omega_q^{01} - \omega_q^{12})/2\pi$ [MHz]	$\chi/2\pi$ [MHz]	$g/2\pi$ [MHz]	$\kappa/2\pi$ [MHz]	$T_1$ [ $\mu\text{s}$ ]	$T_2$ [ $\mu\text{s}$ ]
5.0724	5.7957	$1.38 \times 10^2$	1.100	$2.821 \times 10^1$	$7.205 \times 10^{-1}$	3.0309	1.3503

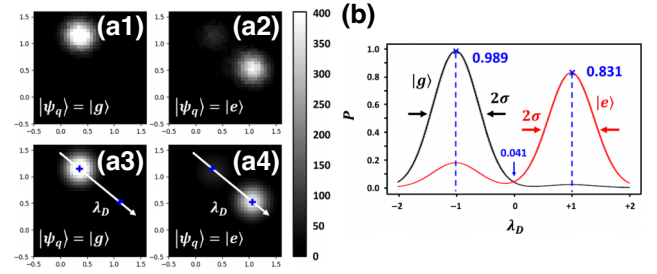


FIG. 4. State-dependent cavity photon responses in the IQ plane and corresponding analysis with 30 000 sampling points. Panels (a-1) and (a-2) depict the populations of readout photons in the IQ plane for the ground and excited qubit state, respectively. Panels (a-3) and (a-4) fit the respective populations with two Gaussian envelopes. We normalize the distance between the two envelopes along the peak-to-peak direction with normalized coordinate  $\lambda_D$ . (b) Plot of normalized populations of readout photons for  $|g\rangle$  (black) and  $|e\rangle$  (red). The standard deviation for each envelope is  $2\sigma = 0.7896$  after normalization. IQ information for each readout photon is converted to a normalized coordinate, and we determine that the state is 0 if  $\lambda_D < \lambda_c$  for an adequate criterion  $\lambda_c$ . Values of the normalized populations for  $\lambda_D = -1, 0, 1$  are written in blue.

Information about the measured photons corresponds to a point on the IQ plane. After the qubit is initialized into  $|g\rangle$  and  $|e\rangle$ , two Gaussian envelopes respectively representing  $|g\rangle$  and  $|e\rangle$  are measured and analyzed by fitting with Python. Then we normalize the population along the normalized coordinate  $\lambda_D$ , as represented in Fig. 4(a).

The selection of the criterion to discriminate between 0 and 1 influences the tomographic results. As measurements that require a finite measurement time, the relaxation, decoherence, and thermal excitation of a qubit provide an inevitable asymmetry of the  $|g\rangle$  and  $|e\rangle$  populations in the IQ plane. The qubit is mostly in its ground state at thermal equilibrium.

The population skewness is parameterized by  $\alpha_{\pm}$  as a function of the selected criterion  $\lambda_c$ , as shown in Fig. 5(a). For the given system, the variance of measured data per measurement number  $N$  follows Eq. (3), so the minimization condition of criterion  $\lambda_c$  is dependent on  $|\psi\rangle_q \in S_B$ . In the present transmon system, optimization of the variance for  $|\psi\rangle_q = |\psi\rangle_{\text{best}}$  or  $|\psi\rangle_q = |\psi\rangle_{\text{worst}}$  is carried out at  $\lambda_c = 0.11$ , which is the general criterion typically used for state readout because it gives the maximum speed of convergence. Each variable described in Figs. 5(b) and 5(c)



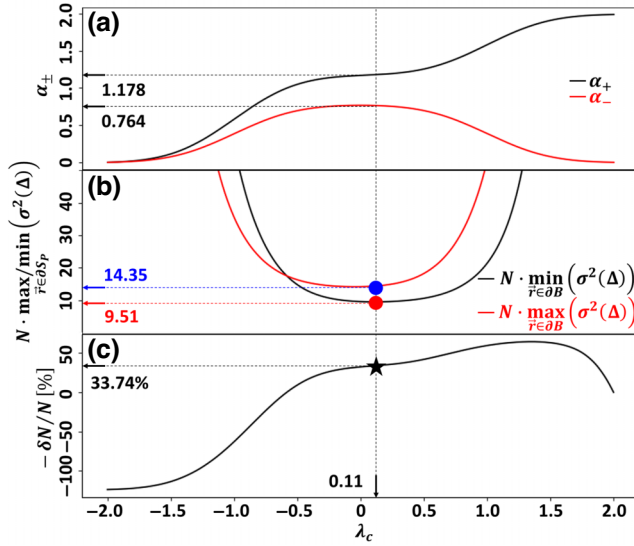


FIG. 5. Calculation process to get a reduced number of required measurements as the criterion  $\lambda_c$  changes. The variables  $\alpha_{\pm}$ , the extremums of variance, and the reduced required number of measurements to get a specific error bound as a function of criterion  $\lambda_c$  are shown. The optimal  $\lambda_c$  that minimizes the minimum variance is 0.11, which is represented as the vertical dashed line. The equations that represent the meanings of the related  $y$  axis are given in each panel. (a) The  $\alpha_-$  variable represents the extent that the two qubit states are decomposed. The  $\alpha_-$  maximum around  $\lambda_c = 0.11$  represents that the two states are well discriminated. (b) Plot of the extremums of variance per data. A crossing is seen at  $\lambda = -0.5828$  where point  $S_{PO}$  crosses point  $P_O$  such that the farthest and nearest points are exchanged. (c) A reduction in the required number of measurement data of around 33.74% at  $\lambda_c = 0.11$  is found. The number of measurement data required to get an equal error bound is proportional to variance  $\sigma^2$  because the statistics for the measurement data follow binomial distribution normalized by  $N$ .

follows

$$\begin{aligned}
 N \cdot \max_{\tilde{r} \in \partial S_P} (\sigma^2(\Delta)) &= \frac{12}{\alpha_-^2} \left[ \frac{3}{4} - 3 \left| \frac{\alpha_+ - \alpha_- / \sqrt{3}}{2} - \frac{1}{2} \right|^2 \right], \\
 N \cdot \min_{\tilde{r} \in \partial S_P} (\sigma^2(\Delta)) &= \frac{12}{\alpha_-^2} \left[ \frac{3}{4} - 3 \left| \frac{\alpha_+ + \alpha_- / \sqrt{3}}{2} - \frac{1}{2} \right|^2 \right], \\
 -\frac{\delta N}{N} &= \frac{\max_{\tilde{r} \in \partial S_P} (\sigma^2(\Delta)) - \min_{\tilde{r} \in \partial S_P} (\sigma^2(\Delta))}{\max_{\tilde{r} \in \partial S_P} (\sigma^2(\Delta))}. \quad (5)
 \end{aligned}$$

At this criterion, the variance per measurement  $[N \times \sigma^2(\Delta)]$  for  $V_{\min}$  is 33.74%, which is smaller than that for  $V_{\max}$ . The number of measured data required to obtain the same error bound is proportional to the variance of the data because QST data follow a binomial distribution, having a variance that is inversely proportional to  $N$ . Therefore, the reduction in the required number of measurements ( $-\delta N/N$ ) is expected to be 33.74% if we drive the qubit

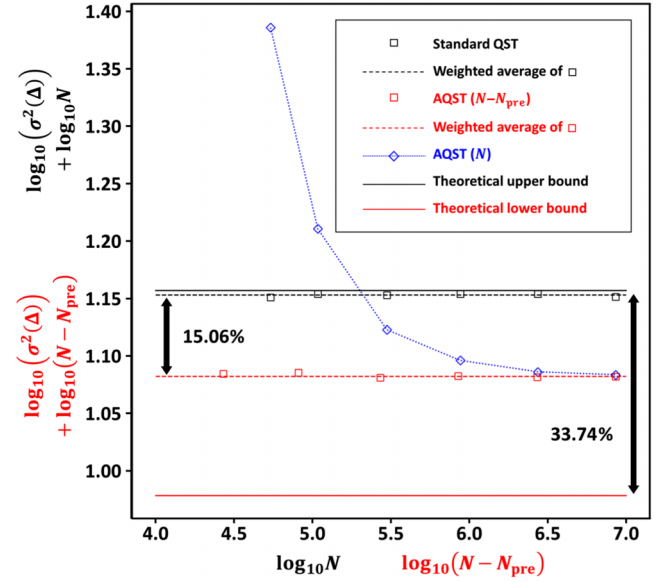


FIG. 6. Convergence of the variance acquired by experiment (square symbols) for standard QST (black) and proposed AQST (red). The graph of variance is normalized by  $\log N$ . We used  $N_{\text{pre}} = 27000$  samples for preestimation, so the data points for AQST are shifted to reflect the computational resources for adaptive feedback (blue). Because  $N_{\text{pre}}$  data for preestimation are not reflected in the total variance, the blue line does not scale as  $O(1/N)$ . To compare the variance of the data from our AQST experiment to the model equation,  $N_{\text{pre}}$  samples are neglected for a pure comparison (red). For both cases of standard QST and AQST, the variances are well fitted along a constant  $y$  line, meaning that they converge with  $1/N$ . The variance decreased by 15.06% for AQST relative to standard QST for both experiment and model. The theoretically expected reduction in variance between the upper and lower bounds for the variance is 33.74%. This theoretical reduction can be accomplished when using a qubit with a long coherence time.

from  $V_{\max}$  to  $V_{\min}$  via feedback; see Appendix E for details. We verified the relative reduction in variance, that is, the relative reduction in the required number of measurements, by comparing the experimental results of standard QST to those of our proposed AQST, as shown in Fig. 6. The first and second line of Eq. (5) show that the variance scales as  $O(1/N)$  for both minimum and maximum variance cases, so the depicted data in the Fig. 6 are log-normalized for a clearer description.

The blue data in Fig. 6 reflect the cost of measurement number  $N_{\text{pre}}$  for preestimation, but they cannot reflect the convergence of postestimation independently. Therefore, additional data points with a subtraction of  $N_{\text{pre}}$  from the number of data  $N$  are plotted in red. The experimental data are plotted with square symbols for both standard QST and AQST schemes. The two dashed horizontal lines are constant  $y$  lines fitted to the data of both schemes. From the difference between the two dashed lines, we

can see a 15.06% reduction in variance for AQST relative to standard QST. Depicted as solid lines in Fig. 6, the theoretically expected reduction is 33.74%, which is the difference between the upper bound (corresponding to  $V_{\max}$ ) and the lower bound (corresponding to  $V_{\min}$ ) of the variance.

This difference between expected and experimental results may derive from two particular characteristics of our experimental setup. The first concerns the small ratio between  $T_2$  and the time for gate operation. The decoherence time ( $T_2 = 1.3503 \mu\text{s}$ ) of our transmon is not long enough to neglect the effect of decoherence during gate operation (180 ns). After providing feedback, we observed a decrease in the purity of the qubit state to 0.70. This was a significant factor contributing to the discrepancy between the  $|\vec{R}|$  in the experimental result and the computed value. The second reason stems from the relatively small number of measurements we carried out for preestimation. As the preestimation step involves a much smaller number of data than the postestimation step, the estimator from the first step was not perfect. Indeed, we found that the estimator from preestimation had errors of around  $5.9^\circ$  in the elevation angle and  $3.2^\circ$  in the azimuth angle of the Bloch sphere.

### III. DISCUSSION

Many studies try to overcome the state-dependent convergence of estimation error in QST by employing the feedback process of AQST. In the same context, the aim of the AQST methodology proposed in this paper is to reduce the error of estimation for the case of an indistinct measurement system. A theoretical investigation of the variance of estimation error gives a minimum variance point  $V_{\min}$  in a probability space  $P$  that is mapped to a state of a qubit  $|\psi\rangle_{\text{best}}$ . The analytically expected reduction in the variance of estimation error by the proposed AQST is 33.74%, which is based on state-dependent cavity photon responses in the IQ plane of Fig. 4. Although the 15.06% reduction observed in our experiment is smaller than that of the analytical expectation, the experimentally achieved reduction can be said to be a significant value. Since enhancing the precision of QST with a finite number of ensembles is an important research topic, the reduction observed from our AQST process can be a meaningful tool for tomography in indistinct measurement systems. Significance also lies in the fact that our approach is not confined to the transmon system presented in this paper; it can be applied to any system with indistinct measurement, making it more universally applicable. As a continuation of this research, by utilizing qubits with various lifetimes and optimizing the measurement pulses, we can get a broader understanding as well as improve the efficiency of our AQST process.

### ACKNOWLEDGMENTS

This work was supported by the National Research Foundation of Korea (NRF) grant funded by Ministry of Science and ICT (MSIT) (No. 2021M3E4A103887713), MSIT ITRC (Information Technology Research Center) support program (IITP-2023-2018-0-01402) supervised by the IITP (Institute for Information & Communications Technology Planning & Evaluation), and Korea Basic Science Institute (KBSI) National Research Facilities & Equipment Center (NFEC) grant funded by the Korean government (Ministry of Science and ICT) (No. PG2022004-09). The JPA used in this paper is supported by Irfan Siddiqi's group at UC Berkeley.

H.H. designed the analytic model, analyzed the data, and wrote the draft of the manuscript; E.S.K. supervised the project and edited the manuscript; H.H. and J.K.C. fabricated the sample and performed experiments. H.H. and J.K.C. contributed equally to this work.

### APPENDIX A: DEFINING THE MAPPING BETWEEN BLOCH SPACE AND PROBABILITY SPACE

A density operator for a state of a single qubit can be denoted by  $\rho = (I + \vec{r} \cdot \vec{\sigma})/2$ , where the vector  $\vec{r} = (r_x, r_y, r_z)$  is a vector in Bloch space that is a unique representation for the state of the qubit with

$$r_k = \langle \sigma_k \rangle = \text{Tr}(\sigma_k \rho). \quad (\text{A1})$$

In this paper, we used three Cartesian axes for tomography. The state of the qubit was rotated by an adequate angle to get three expectation values  $\langle \sigma_k \rangle$  for each  $k$  axis ( $k = x, y, z$ ) as in the following equations:

$$\begin{aligned} \rho_x &= R_y(-\pi/2)\rho R_y(\pi/2), \\ \rho_y &= R_x(\pi/2)\rho R_x(-\pi/2), \\ \rho_z &= \rho. \end{aligned} \quad (\text{A2})$$

As mentioned in the main text, the probability of getting a measurement outcome corresponding to  $j$  for qubit state  $\rho = |i\rangle\langle i|$  is denoted by  $P_i^j$  ( $i \in \{g, e\}, j \in \{0, 1\}$ ). In theory, both  $P_g^0$  and  $P_e^1$  are 1. For a real experiment, however, the relaxation, thermal excitation, and various errors make the probabilities  $P_g^0$  and  $P_e^1$  less than 1. Therefore, we should define the probability of measuring 0 for each axis  $k$  as

$$\begin{aligned} p_k &= P_g^0 \text{Tr}(\hat{P}_g \rho_k) + P_e^0 \text{Tr}(\hat{P}_e \rho_k) \quad \text{where} \\ \hat{P}_i &= |i\rangle\langle i| \quad (i = g, e) \\ &= P_g^0 \left( \frac{1+r_k}{2} \right) + P_e^0 \left( \frac{1-r_k}{2} \right) \\ &= \frac{\alpha_+ + \alpha_- r_k}{2} \quad \text{where } \alpha_{\pm} = P_g^0 \pm P_e^0. \end{aligned} \quad (\text{A3})$$

The above representation can give a useful mapping from Bloch space  $B = \{\vec{r} \mid |r_k| \leq 1, k \in \{x, y, z\}\}$  to probability space  $P = \{\vec{p} = (p_x, p_y, p_z) \mid p_k \in [0, 1], k \in \{x, y, z\}\}$ .

Starting from the above definitions, we can compute the variance of the estimation error from measurement. The estimation error from measurement  $\Delta$  is the difference between  $\hat{r} = (\hat{r}_x, \hat{r}_y, \hat{r}_z)$  and  $\vec{r} = (r_x, r_y, r_z)$ , where  $\hat{r}_k = (2\hat{p}_k - \alpha_+)/\alpha_-$  and  $r_k = (2p_k - \alpha_+)/\alpha_-$  are vectors in Bloch space  $B$  ( $\hat{\cdot}$  means an estimated variable):

$$|\Delta| = \left| \sum_k \hat{k}(\hat{r}_k - r_k) \right| = \frac{2}{\alpha_-} \left| \sum_k \hat{k}(\hat{p}_k - p_k) \right|. \quad (\text{A4})$$

Because the measurements along each axis are independent of each other, and because we consider that the case  $1 - p_k$  does not follow the convergence of  $O(1/N)$  for any  $k$  axis, regardless of how we rotate the qubit state, the variance  $\sigma^2(\Delta)$  is

$$\begin{aligned} \sigma^2(\Delta) &= \sigma^2\left(\frac{2}{\alpha_-} \sum_k \hat{k}(\hat{p}_k - p_k)\right) \\ &= \frac{4}{\alpha_-^2} \sigma^2\left(\sum_k \hat{k}(\hat{p}_k - p_k)\right) \\ &= \frac{4}{\alpha_-^2} \sum_k \frac{p_k(1-p_k)}{N/3} = \frac{12}{N\alpha_-^2} \left(\frac{3}{4} - |\vec{R}|^2\right) \\ &= O\left(\frac{1}{N}\right) \quad \text{where } \vec{R} = \left| \vec{p} - \overrightarrow{OP_O} \right|, \overrightarrow{OP_O} \\ &= \left(\frac{1}{2}, \frac{1}{2}, \frac{1}{2}\right). \end{aligned} \quad (\text{A5})$$

On the other hand, if  $1 - p_k$  follows the convergence of  $O(1/N)$  for a specific axis, it has a different convergence of  $\Delta \sim O(1/N^2)$ , which is explored in Ref. [19]. The point  $P_O$  used in the vector  $\overrightarrow{OP_O}$  is the center of probability space  $P$  (see Fig. 2).

Let us consider a Bloch sphere mapped into probability space denoted by  $S_P$ . The sphere is constructed by vectors  $\vec{p} = (\alpha_+ + \alpha_- r_k)/2$ , so the center of the sphere  $S_P$  is  $S_{PO}(\alpha_+/2, \alpha_+/2, \alpha_+/2)$ . Because  $\alpha_+$  is naturally larger than 1 due to relaxation, the center of the Bloch sphere is closer to  $(1, 1, 1)$  than to  $(0, 0, 0)$ . This means that the distance  $|\vec{R}|$  from a point in the Bloch sphere to  $P_O$  is minimized when  $\vec{p} = ((\alpha_+ - \alpha_-/\sqrt{3})/2)(1, 1, 1) = V_{\max}$  and maximized when  $\vec{p} = ((\alpha_+ + \alpha_-/\sqrt{3})/2)(1, 1, 1) = V_{\min}$  in the probability space (see Fig. 2). The points related to the minimum and the maximum  $|\vec{R}|$  can respectively be

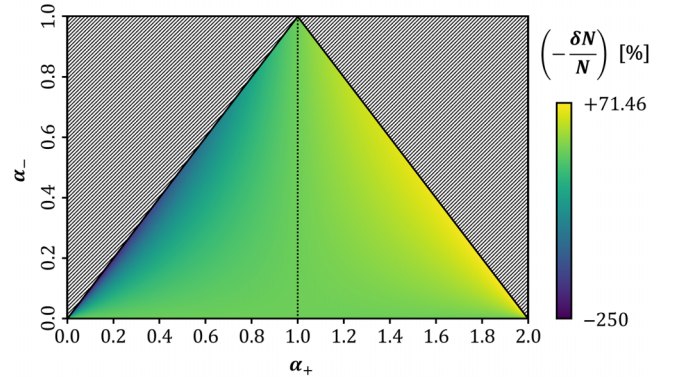


FIG. 7. The reduction in the required number of measurements ( $-\delta N/N$ ) is illustrated as a color map.

expressed as

$$\begin{aligned} |\psi_{\text{worst}}\rangle &= \sqrt{\frac{3-\sqrt{3}}{2}}|0\rangle + e^{i\frac{5\pi}{4}}\sqrt{\frac{3+\sqrt{3}}{2}}|1\rangle, \\ |\psi_{\text{best}}\rangle &= \sqrt{\frac{3+\sqrt{3}}{2}}|0\rangle + e^{i\frac{\pi}{4}}\sqrt{\frac{3-\sqrt{3}}{2}}|1\rangle. \end{aligned} \quad (\text{A6})$$

If we compare the worst and the best state, the reduction in the required number of measurements ( $-\delta N/N$ ), shown in Figure 7, is given by

$$\begin{aligned} N \cdot \max_{\vec{r} \in \partial S_P} (\sigma^2(\Delta)) &= \frac{12}{\alpha_-^2} \left[ \frac{3}{4} - 3 \left| \frac{\alpha_+ - \alpha_-/\sqrt{3}}{2} - \frac{1}{2} \right|^2 \right], \\ N \cdot \min_{\vec{r} \in \partial S_P} (\sigma^2(\Delta)) &= \frac{12}{\alpha_-^2} \left[ \frac{3}{4} - 3 \left| \frac{\alpha_+ + \alpha_-/\sqrt{3}}{2} - \frac{1}{2} \right|^2 \right], \\ \left( -\frac{\delta N}{N} \right) &= \frac{\max_{\vec{r} \in \partial S_P} (\sigma^2(\Delta)) - \min_{\vec{r} \in \partial S_P} (\sigma^2(\Delta))}{\max_{\vec{r} \in \partial S_P} (\sigma^2(\Delta))} \\ &= 1 - \frac{1 - |\alpha_+ + \alpha_-/\sqrt{3} - 1|^2}{1 - |\alpha_+ - \alpha_-/\sqrt{3} - 1|^2}. \end{aligned} \quad (\text{A7})$$

## APPENDIX B: ESTIMATION OF FREQUENCY PARAMETERS

From a single-tone spectroscopy, we can get a dressed cavity spectrum of our qubit-cavity system (Fig. 8). The dressed frequency  $\omega_c^g$  of the cavity for the ground state qubit is 5.072 413 GHz. The transition frequency  $\omega_q$  of our transmon qubit is 5.7957 GHz, the anharmonicity  $\alpha/2\pi$  is 138 MHz, and the Stark shift  $\chi/2\pi$  of our system is 1.100 MHz, which is estimated from the result of two-tone spectroscopy (Fig. 9).

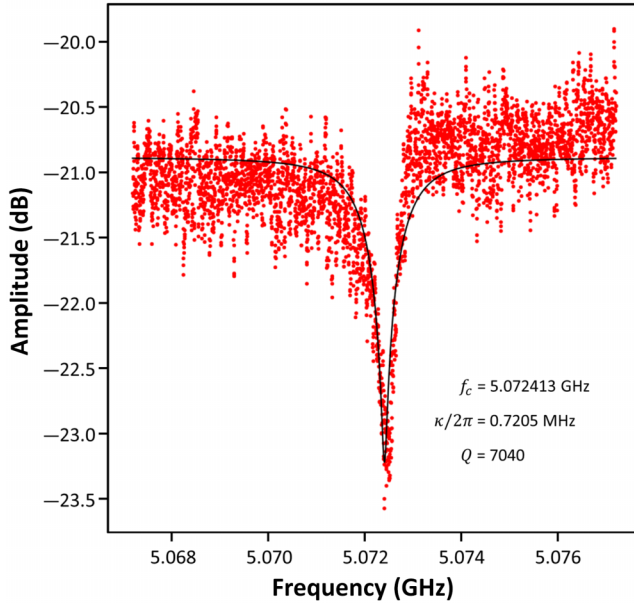


FIG. 8. Single-tone spectroscopy with sufficiently low power to avoid punchout of the cavity.

The characteristic times  $T_1$  and  $T_2$  of our qubit system are estimated from two respective experiments. First, the qubit is initialized in the excited state, and we measure the state after a short delay time. Then we can observe the qubit relaxation and estimate  $T_1$  as  $3.0309 \mu\text{s}$ . Second, we sweep the delay time between two  $\pi/2$ -rotation pulses.

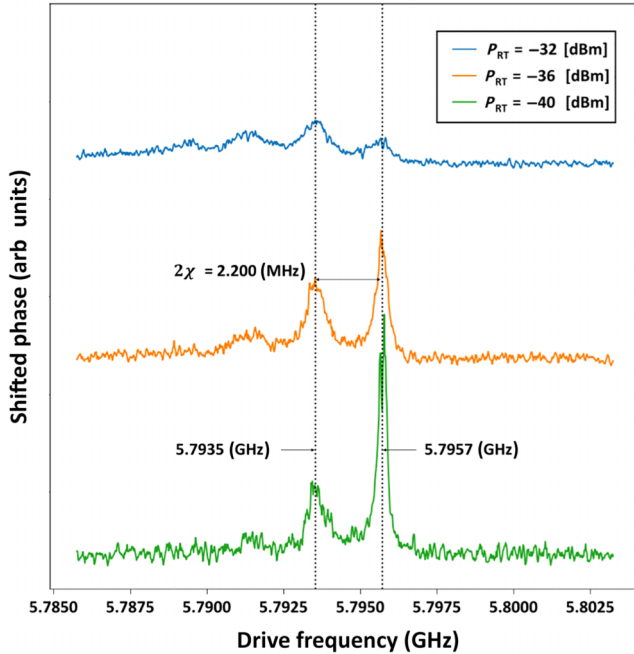


FIG. 9. Two-tone spectroscopy with cavity drive at 5.072 413 GHz varying the measurement power.

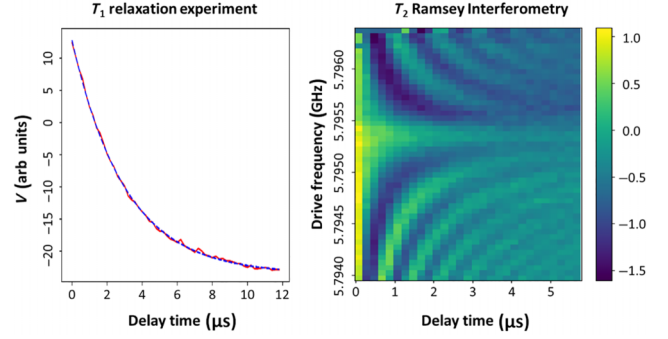


FIG. 10. Measurement data of characteristic times  $T_1$  and  $T_2$ .

In this experiment, we get a qubit decoherence time  $T_2$  of  $1.3503 \mu\text{s}$  (Fig. 10).

### APPENDIX C: MEASUREMENT PROCESS AND FIDELITY

The Jaynes-Cummings model is described in the dispersive limit

$$H = \frac{1}{2} \hbar \omega_q \sigma_z + \hbar \omega_a a^\dagger a + \hbar \chi a^\dagger a \sigma_z. \quad (\text{C1})$$

The last term of Eq. (C1) corresponds to the interaction between the qubit and cavity, which commutes with both  $n = a^\dagger a$  and  $\sigma_z$ . The commuting property gives the possibility for a quantum nondemolition measurement that allows the measurement of both  $n$  and  $\sigma_z$  not to disturb the quantum state.

The average photon number  $\bar{n}$  can be estimated using the critical photon number  $n_{\text{crit}} = \Delta^2/4g^2$  of the system. The characteristic measurement time  $\tau_m$  can be estimated by analyzing the distribution in the IQ plane with a model of discrepancy  $S = \Delta V^2/\sigma^2 = 4T/\tau_m$  [19].

Let us find the variables mentioned in the above paragraph. The critical photon number of our system is  $n_{\text{crit}} = \Delta^2/4g^2 = 164.35$ , which corresponds to  $-34$  dBm at the 300 K stage as we observed the dispersive approximation breaks down. Because our measurement signal has  $-38$  dBm at the 300 K stage, we can infer that  $\bar{n} = 65.43$  [41]. Also, from the measurement time  $T = 1 \mu\text{s}$  and the discrepancy  $S = 1.604$  fitted by Python using IQ distribution data (see Fig. 11), we can get  $\tau_m \simeq 2.494 \mu\text{s}$ .

### APPENDIX D: CAVITY PHOTON READOUT AND DISTRIBUTION IN IQ PLANE

In this section we aim to analyze the distribution of cavity photons. When we plot the reference data for the ground and excited states on a log scale, they appear as shown in Figure 11. We were able to confirm the shape of the  $f$  state as mentioned by the referee. Furthermore, we observed that the size of these data was approximately 3 points per bin,



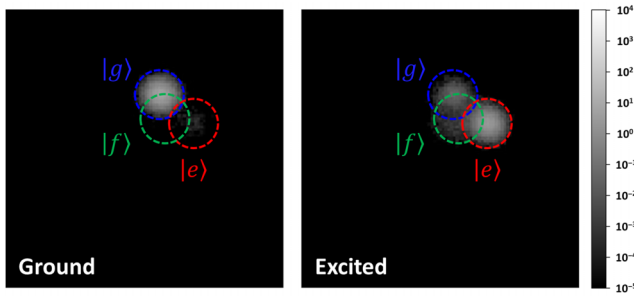


FIG. 11. The reference data for the ground and excited states on a log scale. Three envelopes are observed: ground state (blue), excited state (red), and second excited state (green).

which is approximately 0.75% of the size of the peak at 398 points per bin. This  $f$ -state population can affect the error of estimation and the skewness of the statistics in the data.

### APPENDIX E: CRITICAL NUMBER OF ENSEMBLE

In our AQST process, there is a specific “cost” associated with preestimation. Here, we focus on a crucial of ensemble number threshold, where the efficiency of AQST surpasses that of standard QST. The critical number of ensembles, denoted by  $N_c$ , can be defined using the following equation. For ease of calculation, assuming that the preestimation error is sufficiently small ( $N_{\text{pre}} > 10^4$ ) and that all operations have high fidelity, the value of  $N_c$  can be expressed as a solution to the equation involving  $NL$

$$\min_{\vec{r} \in \partial S_P} (\sigma^2(\Delta)) / (N - N_{\text{pre}}) = \max_{\vec{r} \in \partial S_P} (\sigma^2(\Delta)) / N$$

$$\rightarrow 1 - \frac{N_{\text{pre}}}{N} = \frac{1 - \left| \alpha_+ + \frac{\alpha_-}{\sqrt{3}} - 1 \right|^2}{1 - \left| \alpha_+ - \frac{\alpha_-}{\sqrt{3}} - 1 \right|^2}. \quad (\text{E1})$$

For our specific system, the critical number is approximately 168 000, whereas the value obtained from the above equation is roughly 80 000. This difference arises from decoherence caused by a low  $T_2$  value. Subsequent to the preparation of the ensemble initialized in  $|\psi_{\text{worst}}\rangle$ , the qubit state experiences a loss of coherence over a 180 ns feedback period. The decoherence amount, about 87% for each 180 ns (calculated from  $T_2 = 1.305 \mu\text{s}$ ), has been experimentally verified by the 70% reduction in  $|\vec{r}|$ . The computed value and the estimated value show a discrepancy of around 80%, attributable to additional decoherence occurring during three 60-ns gate operations for feedback. Consequently, the state does not reside precisely on the shell of the Bloch sphere, leading to a distance  $|\vec{R}|$  of 0.39

(estimated from the AQST result) rather than 0.53 (the calculated value for  $|\psi_{\text{best}}\rangle$ ).

- [1] W. Band and J. L. Park, The empirical determination of quantum states, *Found. Phys.* **1**, 133 (1970).
- [2] D. F. V. James, P. G. Kwiat, W. J. Munro, and A. G. White, Measurement of qubits, *Phys. Rev. A* **64**, 052312 (2001).
- [3] U. Fano, Description of states in quantum mechanics by density matrix and operator techniques, *Rev. Mod. Phys.* **29**, 74 (1957).
- [4] M. Paris and J. Rehacek, *Quantum State Estimation* (Springer Science & Business Media, 2004), Vol. 649.
- [5] R. Schmied, Quantum state tomography of a single qubit: comparison of methods, *J. Mod. Opt.* **63**, 1744 (2016).
- [6] K. Vogel and H. Risken, Determination of quasiprobability distributions in terms of probability distributions for the rotated quadrature phase, *Phys. Rev. A* **40**, 2847 (1989).
- [7] U. Leonhardt and H. Paul, Measuring the quantum state of light, *Prog. Quantum Electron.* **19**, 89 (1995).
- [8] Z. Hradil, Quantum-state estimation, *Phys. Rev. A* **55**, R1561 (1997).
- [9] K. R. W. Jones, Principles of quantum inference, *Ann. Phys. (N.Y.)* **207**, 140 (1991).
- [10] K. R. W. Jones, Fundamental limits upon the measurement of state vectors, *Phys. Rev. A* **50**, 3682 (1994).
- [11] K. R. W. Jones, Quantum limits to information about states for finite dimensional Hilbert space, *J. Phys. A* **24**, 121 (1991).
- [12] T. Sugiyama, P. S. Turner, and M. Muraio, Effect of non-negativity on estimation errors in one-qubit state tomography with finite data, *New J. Phys.* **14**, 085005 (2012).
- [13] M. D. de Burgh, N. K. Langford, A. C. Doherty, and A. Gilchrist, Choice of measurement sets in qubit tomography, *Phys. Rev. A* **78**, 052122 (2008).
- [14] R. D. Gill and S. Massar, State estimation for large ensembles, *Phys. Rev. A* **61**, 042312 (2000).
- [15] O. E. Barndorff-Nielsen and R. D. Gill, Fisher information in quantum statistics, *J. Phys. A: Math. General* **33**, 4481 (2000).
- [16] F. Embacher and H. Narnhofer, Strategies to measure a quantum state, *Ann. Phys. (N.Y.)* **311**, 220 (2004).
- [17] Y. Lu and Q. Zhao, Minimum copies of Schrödinger’s cat state in the multi-photon system, *Sci. Rep.* **6**, 1 (2016).
- [18] R. Bianchetti, S. Filipp, M. Baur, J. M. Fink, C. Lang, L. Steffen, M. Boissonneault, A. Blais, and A. Wallraff, Control and tomography of a three level superconducting artificial atom, *Phys. Rev. Lett.* **105**, 223601 (2010).
- [19] S. J. Weber, A. Chantasri, J. Dressel, A. N. Jordan, K. W. Murch, and I. Siddiqi, Mapping the optimal route between two quantum states, *Nature* **511**, 570 (2014).
- [20] S. S. Straupe, Adaptive quantum tomography, *Sov. J. Exp. Theor. Phys. Lett.* **104**, 510 (2016).
- [21] D. H. Mahler, L. A. Rozema, A. Darabi, C. Ferrie, R. Blume-Kohout, and A. M. Steinberg, Adaptive quantum state tomography improves accuracy quadratically, *Phys. Rev. Lett.* **111**, 183601 (2013).

- [22] R. Blume-Kohout, Optimal, reliable estimation of quantum states, *New J. Phys.* **12**, 043034 (2010).
- [23] F. Huszár and N. M. T. Houlby, Adaptive Bayesian quantum tomography, *Phys. Rev. A* **85**, 052120 (2012).
- [24] K. S. Kravtsov, S. S. Straupe, I. V. Radchenko, N. M. T. Houlby, F. Huszár, and S. P. Kulik, Experimental adaptive bayesian tomography, *Phys. Rev. A* **87**, 062122 (2013).
- [25] J. Řeháček, B.-G. Englert, and D. Kaszlikowski, Minimal qubit tomography, *Phys. Rev. A* **70**, 052321 (2004).
- [26] B. Qi, Z. Hou, Y. Wang, D. Dong, H. S. Zhong, L. Li, G. Y. Xiang, H. M. Wiseman, C. F. Li, and G. C. Guo, Adaptive quantum state tomography via linear regression estimation: Theory and two-qubit experiment, *npj Quantum Inf.* **3**, 19 (2017).
- [27] E. Bagan, M. A. Ballester, R. D. Gill, R. Muñoz Tapia, and O. Romero-Isart, Separable measurement estimation of density matrices and its fidelity gap with collective protocols, *Phys. Rev. Lett.* **97**, 130501 (2006).
- [28] X. Zhu, Y. Deng, R. Gao, Q. Wei, L. Liu, and Z. Luo, Adaptive quantum state tomography via weak value, *Results Phys.* **31**, 104999 (2021).
- [29] W. K. Wootters and B. D. Fields, Optimal state-determination by mutually unbiased measurements, *Ann. Phys. (N.Y.)* **191**, 363 (1989).
- [30] C. W. Wu, J. Zhang, Y. Xie, B. Q. Ou, T. Chen, W. Wu, and P. X. Chen, Scheme and experimental demonstration of fully atomic weak-value amplification, *Phys. Rev. A* **100**, 62111 (2019).
- [31] S. Wu and Y. Li, Weak measurements beyond the Aharonov-Albert-Vaidman formalism, *Phys. Rev. A—At., Mol., Opt. Phys.* **83**, 1 (2011).
- [32] R. Jozsa, Complex weak values in quantum measurement, *Phys. Rev. A—At., Mol., Opt. Phys.* **76**, 1 (2007).
- [33] L. Qin, L. Xu, W. Feng, and X. Q. Li, Qubit state tomography in a superconducting circuit via weak measurements, *New J. Phys.* **19**, 033036 (2017).
- [34] M. Kjaergaard, M. E. Schwartz, J. Braumüller, P. Krantz, J. I. Wang, S. Gustavsson, and W. D. Oliver, Superconducting qubits: current state of play, *Annu. Rev. Condens. Matter Phys.* **11**, 369 (2020).
- [35] J. Koch, T. M. Yu, J. Gambetta, A. A. Houck, D. I. Schuster, J. Majer, A. Blais, M. H. Devoret, S. M. Girvin, and R. J. Schoelkopf, Charge-insensitive qubit design derived from the Cooper pair box, *Phys. Rev. A* **76**, 1 (2007).
- [36] J. A. Schreier, A. A. Houck, J. Koch, D. I. Schuster, B. R. Johnson, J. M. Chow, J. M. Gambetta, J. Majer, L. Frunzio, M. H. Devoret, S. M. Girvin, and R. J. Schoelkopf, Suppressing charge noise decoherence in superconducting charge qubits, *Phys. Rev. B* **77**, 2 (2008).
- [37] G. Wendin, Quantum information processing with superconducting circuits: A review, *Rep. Progr. Phys.* **80**, 1 (2017).
- [38] C. K. Andersen and A. Blais, Ultrastrong coupling dynamics with a transmon qubit, *New J. Phys.* **19**, 1 (2017).
- [39] L. Chen, H.-X. Li, Y. Lu, C. W. Warren, C. J. Kri, S. Kosen, M. Rommel, S. Ahmed, A. Osman, J. Biznárová, A. F. Roudsari, B. Lienhard, M. Caputo, K. Grigoras, L. Grönberg, J. Govenius, A. F. Kockum, P. Delsing, and J. Bylander, Transmon qubit readout fidelity at the threshold for quantum error correction without a quantum-limited amplifier, *npj Quantum Inf.* **9**, 1 (2023).
- [40] H. Paik, D. I. Schuster, L. S. Bishop, G. Kirchmair, G. Catelani, A. P. Sears, B. R. Johnson, M. J. Reagor, L. Frunzio, L. I. Glazman, S. M. Girvin, M. H. Devoret, and R. J. Schoelkopf, Observation of high coherence in Josephson junction qubits measured in a three-dimensional circuit QED architecture, *Phys. Rev. Lett.* **107**, 240501 (2011).
- [41] J. Gambetta, A. Blais, D. I. Schuster, A. Wallraff, L. Frunzio, J. Majer, M. H. Devoret, S. M. Girvin, and R. J. Schoelkopf, Qubit-photon interactions in a cavity: Measurement-induced dephasing and number splitting, *Phys. Rev. A* **74**, 042318 (2006).
- [42] J. Koch, T. M. Yu, J. Gambetta, A. A. Houck, D. I. Schuster, J. Majer, A. Blais, M. H. Devoret, S. M. Girvin, and R. J. Schoelkopf, Charge-insensitive qubit design derived from the Cooper pair box, *Phys. Rev. A* **76**, 042319 (2007).
- [43] E. Jeffrey, D. Sank, J. Y. Mutus, T. C. White, J. Kelly, R. Barends, Y. Chen, Z. Chen, B. Chiaro, A. Dunsworth, A. Megrant, P. J. J. O’Malley, C. Neill, P. Roushan, A. Vainsencher, J. Wenner, A. N. Cleland, and J. M. Martinis, Fast accurate state measurement with superconducting qubits, *Phys. Rev. Lett.* **112**, 190504 (2014).

*Correction:* The Acknowledgment section contained incorrect information and has been fixed. The statement regarding author contributions contained an omission and has been amended. All previously published figures have been replaced to fix issues regarding the appearance of the fonts.